Nature Communications

https://doi.org/10.1038/s41467-026-69906-y

Article in Press

Giant photostriction rate for remote opto-ultrasonic structural health monitoring

Received: 31 July 2025

Accepted: 12 February 2026

Cite this article as: Yin, J., Yang, Y., Shi, X. *et al.* Giant photostriction rate for remote opto-ultrasonic structural health monitoring. *Nat Commun* (2026). https://doi.org/10.1038/s41467-026-69906-y

Jie Yin, Yuxuan Yang, Xiaoming Shi, Chunlin Zhao, Cong Lin, Hong Tao, Yang Zhang, David Boon Kiang Lim, Chao Jiang, Liming Lei, Yunfeng Song, Haijun Wu, Xiangdong Ding, Jun Sun, Fei Li, Jiagang Wu & Kui Yao

Giant Photostriction Rate for Remote Opto-ultrasonic Structural Health Monitoring

Jie Yin[✉,1,2], Yuxuan Yang[3], Xiaoming Shi[4], Chunlin Zhao[5], Cong Lin[5], Hong Tao[6], Yang Zhang[3], David Boon Kiang Lim[2], Chao Jiang[2], Liming Lei[7], Yunfeng Song[8], Haijun Wu[✉,3], Xiangdong Ding[3], Jun Sun[3], Fei Li[✉,3], Jiagang Wu[✉,1], Kui Yao[✉,2]

Abstract:

Extending photocarrier lifetime, accelerating photostrictive strain buildup, and engaging more light–lattice interactions are essential to increase the bulk photostriction rate—a key figure of merit integrating strain magnitude and generation speed (typically < 10^{-3} s^{-1} in bulk ferroelectrics)—for efficient remote ultrasound generation. Here, we report non-poled terbium-doped (K,Na)NbO_3 ceramics, where Tb^{3+} 4*f*-electron trapping prolongs photocarrier lifetime, enabling efficient carrier drift to domain walls for screening depolarization field. Hierarchical nanostructures—dense nanodomains (accelerating photostriction via coupled local bulk photovoltaic and converse piezoelectric effects) and subwavelength grains (more light–lattice interactions and enhancing collective photostriction)—yield an outstanding bulk photostriction rate of 6.41×10^{-1} s^{-1}, two orders above conventional bulk ferroelectrics. Non-poled ceramics avoid depoling issue, enabling robust and low power opto-ultrasonic transducers for reliable remote structural health monitoring. Our bulk ferroelectric design strategy enables cost-effective, high-performance opto-ultrasonic sensing technologies.

[1]College of Physics, Sichuan University, Chengdu, China. [2]Institute of Materials Research and Engineering, Agency for Science, Technology and Research (A*STAR), Singapore. [3]State Key Laboratory for Mechanical Behavior of Materials, Electronic Materials Research Laboratory (Key Lab of Education Ministry) and School of Electronic and Information Engineering, Xi’an Jiaotong University, Xi’an 710049, China. [4]School of Mathematics and Physics, University of Science and Technology Beijing, Beijing, China. [5]College of Materials Science and Engineering, Fuzhou University, Fuzhou, China. [6]Physics Department, Southwest Minzu University, Chengdu, China. [7]TaiHang Laboratory, Chengdu, China. [8]Zhejiang Shunhui Optical Technology Co., Ltd, Hangzhou, China. Corresponding author: m15608012851@163.com, wuhaijunnavy@xjtu.edu.cn, ful5@xjtu.edu.cn, msewujg@scu.edu.cn, yao_kui@a-star.edu.sg

Introduction

Elastic waves, governed by coupled stress-strain dynamics and wave-matter interactions, facilitate acoustic information and energy transfer, underpinning applications in non-destructive testing/evaluation (NDT/NDE), biosensing, signal processing, and wave-based computing[1]. Conventional systems rely on wired acoustic transducers, whereas remote, contact-free operation is essential for inaccessible environments, to minimize invasive mass, electromagnetic interference, system complexity and cost. Optomechanical energy conversion, where light drives mechanical vibration, provides such a solution and advances applications in actuation[2-4], imaging[5,6], sensing[7,8], and quantum technologies[9,10]. Potential mechanisms include deformation-potential coupling[11], magnetostriction[12,13], stimulated Brillouin scattering[14,15], thermoelastic expansion[16,17], molecular or electronic structural transitions[18,19], and ferroelectric photostriction[20,21]. While deformation-potential, magnetostrictive, and Brillouin scattering allow ultrafast but nanoscale phonon generation, their limited active volume hinders macroscopic ultrasound production. Thermoelastic expansion is straightforward yet with low efficiency (10^{-6}–10^{-8}) [22, 23], requiring high-power pulsed lasers. Molecular phase transitions offer large strains (5–20%) but exhibit slow kinetics (seconds scale) and irreversibility[24-29]. Ferroelectric photostriction—initiated by photocarrier separation, drift to and accumulation at domain walls, and the resultant screening of bound charges that produces local fields which, generate domain-scale strain via the converse piezoelectricity (Fig. 1a)[20,21]—offers a reversible, cost-effective and low peak-power way for scalable opto-ultrasonic actuation.

Large and fast photostriction at microscale level, such as at lattice structure, was reported in ferroelectric materials, but not adequately manifested at macroscale. This hinders sufficient acoustic pressure generation and elastic-wave coupling efficiency, motivating the pursuit of macroscale large and fast photostriction in bulk ferroelectrics. However, bulk systems inherently suffer from inefficient carrier drift (rapid photocarrier recombination), slow photovoltage buildup (milliseconds to seconds), and poor light penetration (~tens of nm under above-bandgap excitation), collectively suppressing their photostriction rate—an ultrasonic device-level figure of merit integrating strain magnitude and response speed—to below 10^{-3} s^{-1}, insufficient for efficient opto-mechanical ultrasound generation[22,30-34]. Moreover, the complexity of electrical poling and susceptibility to depoling during prolonged operation limit the robustness and reliability of poled bulk ferroelectrics for long-term remote opto-ultrasonic applications. Overcoming these challenges requires improved drift efficiency (prolonging photocarrier lifetime), localized optomechanical coupling (accelerating the domain-scale strain without poling), and enhanced light penetration (activating more grains).

Here, we show a hierarchical structural design strategy, to achieve a giant photostriction rate in bulk

ferroelectrics. By tailoring sub-wavelength grain sizes to minimize Rayleigh scattering, we enhance optical penetration for maximizing light-lattice interactions and enhancing the collective photostriction (Fig. 1b). Within these grains, nano-domain architectures are configured for enabling fast local photostriction. Phase-field simulations reveal that photocarrier drift and accumulation in properly nano-sized domains efficiently screens the depolarization field at domain walls, generating local strains that can accumulate constructively into collective photostriction without poling treatment (Fig. 1c). Moreover, we strategically introduce heavy terbium dopants (Tb^{3+}) to create electron traps via densely split 4*f*-electron levels, prolonging photocarrier lifetimes[35], enhancing carrier drift efficiency toward domain walls, thereby amplifying the local photostriction (Fig. 1d). A larger spontaneous polarization magnitude (P_{mag}) facilitates photocarrier separation, while a greater polarization angle deviation (*DP*) signifies reduced domain size[36], collectively leading to enhanced local photostriction. In perovskite ABO_3 displacive ferroelectrics, spontaneous polarization (P_s) primarily arises from the relative displacement of B-site cations against the oxygen octahedral center. To achieve a relatively large P_{mag} while introducing strong random fields for a substantial *DP*, we employed A-site Tb^{3+} doping.

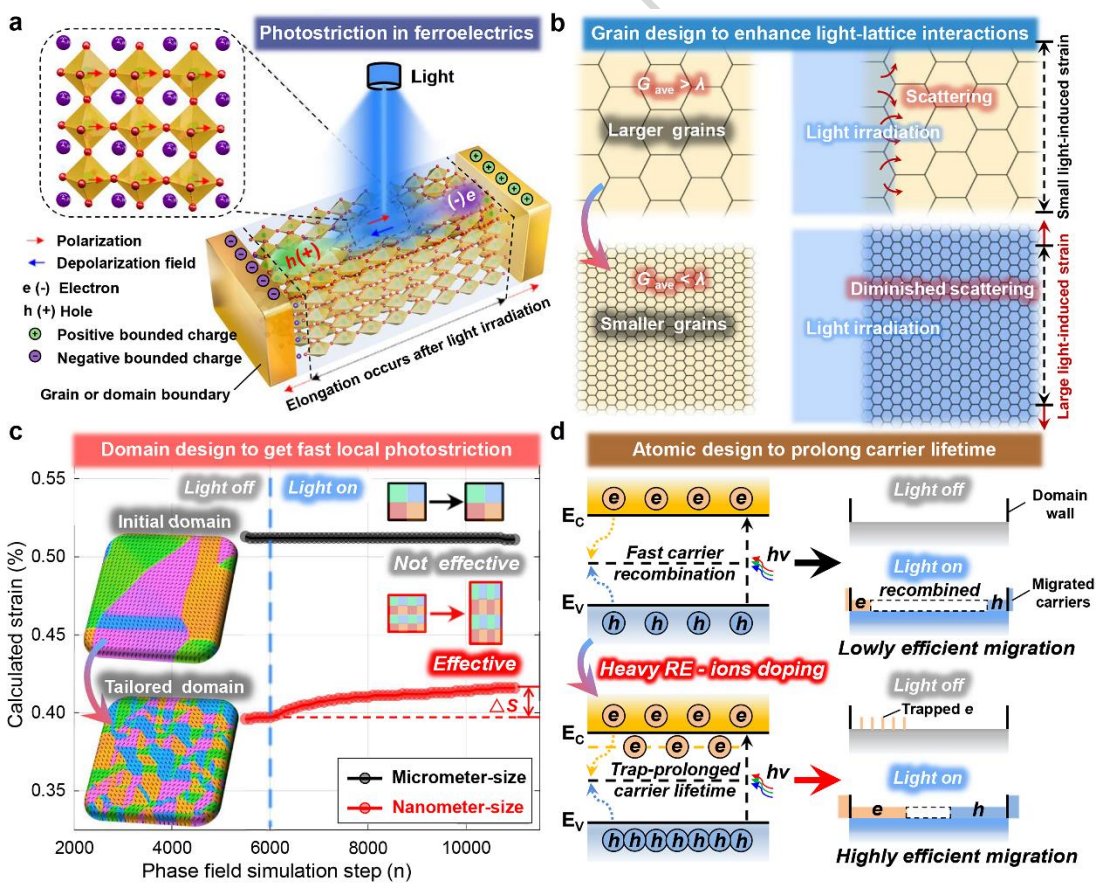

Fig. 1 | Hierarchical design strategy for enhancing the photostriction rate in bulk ferroelectrics. a, Schematic of photostriction in ferroelectrics. Photocarrier drift under the spontaneous polarization aligned

internal electric field, enables photo-induced strain via the converse piezoelectric response to charge redistribution. **b**, Grain-level design to enhance light-lattice interactions. Large grains scatter light at grain boundaries, reducing transmittance. Decreasing grain size below the light wavelength minimizes scattering, improving light penetration, and enhances light-lattice interaction. **c**, Domain-level design for rapid local photostriction. Phase-field simulations incorporating carrier drift within domains reveal optimized domain size for enhancing local photostriction in bulk ferroelectrics. **d**, Atomic-level design for prolonged carrier lifetime and efficient carrier drift to domain walls. Rare-earth (RE) element terbium (Tb) is introduced as the donor dopant, to create optimal electron traps via densely split 4*f*-electron levels. These traps extend carrier lifetime and facilitate drift toward domain walls, enhancing local photostriction.

Leveraging these principles, we doped Tb^{3+} at A-sites within lead-free KNN ceramics- a widely studied and highly tunable ferroelectric platform—to simultaneously engineer grain size, domain architecture, and atomic-level structures as envisioned in our design. The resultant non-poled KNN-Tb ceramics exhibit an outstanding bulk photostriction rate of 6.41×10^{-1} s^{-1}, two orders of magnitude higher than the reported ferroelectric photostriction in the literature, such as $Pb(Mg_{1/3}Nb_{2/3})O_3$-$PbTiO_3$ (PMN-PT) and $BiFeO_3$ (BFO) single crystals. Atomic-scale structural analysis reveals underlying structural driving forces underlying the exceptional performance. Intensive ultrasonic waves were excited by light and reliable remote SHM function was demonstrated, using an opto-ultrasonic cantilever transducer made from the non-poled KNN-Tb. Crucially, the non-poled nature of KNN-Tb simplifies device fabrication, avoids depoling issues during prolonged operation, and enhances reliability and durability, marking a critical advancement toward next-generation opto-ultrasonic devices for practical applications.

Results and Discussion

Enhanced Optical Transmittance and Enhanced Photostriction in KNN-Tb

We optimized the fabrication process of KNN-*x*Tb (*x*=0, 0.01, 0.02, 0.03, 0.04) ceramics (Supplementary Methods 1.1), to prepare ferroelectric ceramics with reduced optical scattering and improved transmission in the visible light spectrum, and thus the samples show transparency. Representative samples (*x*=0.01, 0.02, 0.03) were selected to show their optical transmittance from 300 nm to 800 nm, as provided in Fig. 2a. Specifically, the transmittance of KNN-*x*Tb ceramics at the 400 nm excitation wavelength were evaluated, revealing that the increased transmittance at this wavelength significantly boosts photo-induced photovoltage (Fig. 2b and Supplementary Fig. S1). To eliminate compositional effects on the photovoltage, we analyzed the photovoltage of KNN-0.02Tb ceramics produced under varying processing conditions (Supplementary Fig. S2), revealing a proportional relationship between transmittance at the 400 nm excitation wavelength and photovoltage.

Additionally, our investigations into photo-induced displacement of KNN-*x*Tb cantilevers, encompassing both poled and non-poled samples, demonstrated that non-poled samples can excite significant photo-

induced displacement responses, as provided in Fig. 2c. Notably, the non-poled KNN–0.02Tb ceramic cantilever achieved a maximum photostrictive displacement of 202 nm, markedly surpassing that of a commercial PMN–PT single crystal cantilever (~3 nm) with identical dimensions. All photostriction measurements on KNN–Tb ceramics and PMN–PT single crystals were performed under identical above-band-gap excitation conditions (same 400 nm illumination laser with the same photon flux and geometry), ensuring a consistent electromagnetic energy input and the reliable and fair comparison (Supplementary Methods 1.2). While the absolute photoexcited carrier concentration may differ between the two materials due to variations in optical absorption coefficient, carrier lifetime, and defect-related trapping, the photostrictive response in bulk ferroelectrics is also governed by domain-wall-mediated carrier trapping and screening.

Under these identical excitation conditions, KNN–Tb ceramic cantilever exhibits photostriction rate of up to 6.41×10^{-1} s^{-1} (Supplementary Note 1 and Fig. S3), which is nearly two orders of magnitude higher than that in PMN-PT single crystal cantilever (8.06×10^{-3} s^{-1}), as depicted in Fig. 2d. Moreover, our KNN-0.02Tb ceramic sample exhibits robust water resistance, maintaining its photostriction performance even after 30 days of water immersion, as demonstrated by the cantilever with the same size fabricated from the immersed samples (Supplementary Fig. S4). These characteristics highlight the advantage and practical application potential of our KNN–Tb ceramics for opto-ultrasonic transduction.

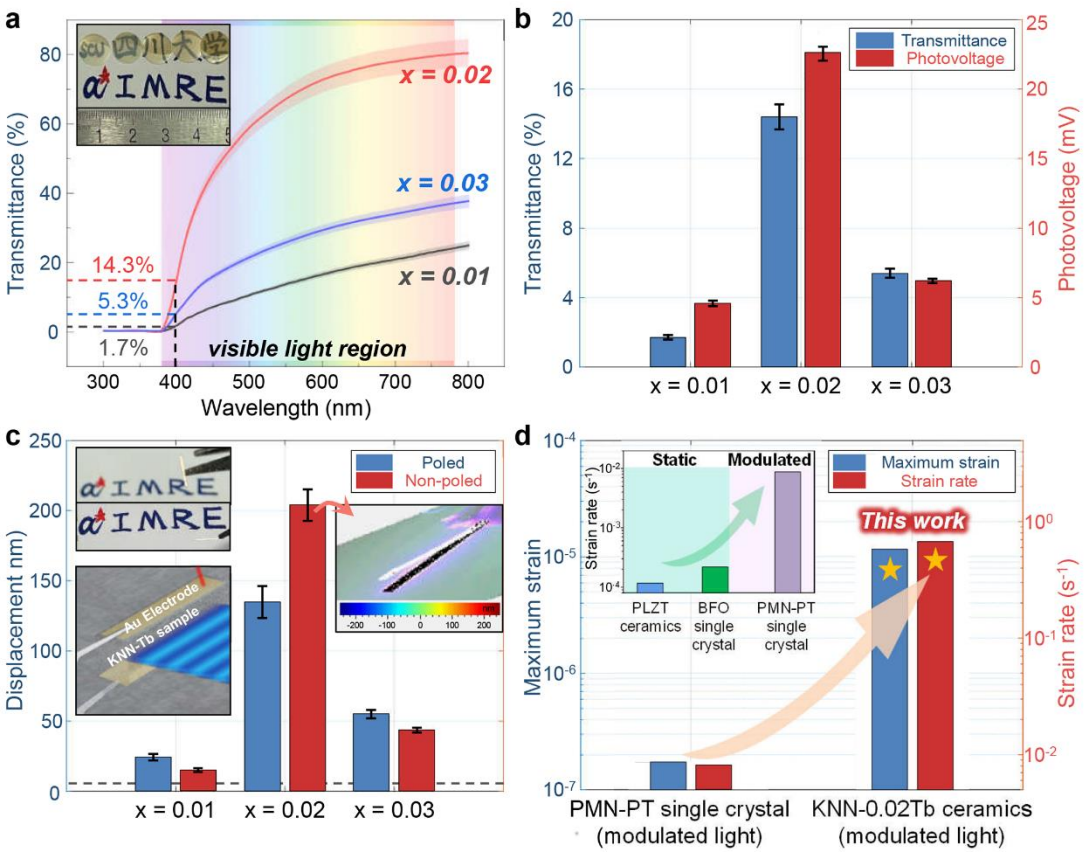

Fig. 2 | Enhanced optomechanical coupling in KNN-Tb ceramics. a, Optical transmittance of KNN-*x*Tb ceramics (*x*=0-0.03) across the 300 nm to 800 nm wavelength range. The error bars are shown as semi-transparent shaded regions around the transmittance curves. **b**, Comparison of transmittance and photovoltage in KNN-*x*Tb (*x*=0-0.03) ceramics, under modulated light with 400 nm wavelength. **c**, Photo-induced displacement in poled and non-poled KNN-*x*Tb (*x*=0-0.03) ceramic cantilevers, under modulated light with 400 nm wavelength. The dashed line represents reference data obtained from a PMN–PT single-crystal cantilever of identical dimensions measured under the same conditions. **d**, Maximum strain and strain rate across representative photostrictive materials, showcasing the substantially enhanced photostrictive strain and strain rate in non-poled KNN-0.02Tb ceramics.

Deciphering Structural Driving Force of Enhanced Photostriction in KNN-Tb

The frequency-dependent electromechanical analysis (Supplementary Notes 2 and 3, Fig. S5) confirms that the large displacement and strain, observed in the KNN-Tb cantilever, originate from electromechanical resonance rather than thermal expansion (Supplementary Note 4 and Fig. S6), consistent with that in PMN-PT crystal cantilevers. To understand why the photostriction rate of KNN-Tb ceramics is two orders of magnitude higher than that of PMN-PT crystals, we analyzed the two key factors in photostriction rate

calculation: resonance frequency and maximum deflected displacement of the cantilever (Supplementary Note 1). Compared with the PMN–PT crystal cantilever of identical dimensions and clamping conditions, the KNN–Tb ceramic cantilever exhibits a higher resonance frequency (9.1 kHz vs. 7.7 kHz). For cantilevers of the same geometry, the fundamental resonance frequency scales as $\sqrt{E/\rho}$ [37], where E is the Young's modulus and ρ is the density, consistent with the difference in E/ρ between the two materials (see Supplementary Note 5 for detailed discussion). Additional factors—including boundary fixation, ceramic porosity, and single-crystal anisotropy—may further contribute to the observed frequency difference[38]. Furthermore, the KNN–Tb cantilever demonstrates a substantially larger maximum deflection (202 nm) than the PMN–PT cantilever (3 nm) under identical conditions, resulting in a markedly enhanced photostrictive rate.

To uncover the microscopic origin of this enhancement, we investigated the structural mechanisms governing the photostriction in KNN-Tb. While a recently proposed unit-cell polarization screening model predicts sub-picosecond photostriction in ferroelectrics[39], our measurements reveal a microsecond-scale delay between peak illumination and maximum strain (Fig. S7), suggesting an obviously different underlying process. Instead, photocarrier drift to local domain walls to screen the depolarization fields model appears to be applicable to our case, as supported by energy conversion analysis: the bulk photovoltaic effect (BPVE) efficiency η_{BPVE}, and photostriction efficiency η_{pho}, are 8.6×10^{-11} and 1.47×10^{-4}, respectively (Supplementary Note 6 and Figs. S8 and S9). While bulk photostriction theory limits η_{pho} to $\eta_{\mathrm{BPVE}} \times \eta_{\mathrm{CPE}}$ (CPE is the converse piezoelectric effect), our results demonstrate that we have overcome this constraint through local opto-electromechanical coupling, manifested as local photostriction. This phenomenon is governed by (1) the magnitude of local electric field variations, driven by photocarrier screening of the depolarization field, and (2) the strength of the local converse piezoelectric effect, determined by the intrinsic lattice properties of the material.

A phase-field model incorporating photocarrier drift (Supplementary 2) reveals that optimized nanoscale domains (tens of nanometers) facilitate carrier drift toward domain walls (Fig. 3a). Carrier accumulation at domain walls effectively screens bound charges, suppressing the depolarization field and strengthening the local electric field. However, at ultra-small domain sizes (a few nanometers), intensified random electric fields disrupt directional carrier drift to screen bound charges, diminishing the local electric field. Experimentally, excessive Tb doping enhances random fields, weakening the ability of photo-induced charge carriers to screen depolarization fields, thereby reducing the local piezoelectric response and ultimately diminishing photostrictive strain. Relaxor ferroelectrics, such as PMN-PT and $(Bi_{0.5}Na_{0.5})TiO_3$ (BNT), exhibit strong random fields arising from substantial ionic valence and radius mismatches at the A/B sites[36, 40, 41], which hinder effective charge screening and ultimately degrade photostrictive performance.

In contrast, compositions with smaller ionic disparities, such as KNN (applied in this work) and $BaTiO_3$, are systems more suitable for achieving strong local photostriction. Future research could explore grain-domain-lattice engineering strategies to further enhance photostriction in these systems. Piezoelectric force microscopy (PFM) and switching spectroscopy PFM (SS-PFM) (Figs. S10, S11) confirm that appropriate Tb doping reduces domain size while enhancing the piezoelectric response up to $x = 0.02$, beyond which excessive doping suppresses ferroelectric polarization and dielectric permittivity (Fig. S12). As summarized in Fig. 3b, the optimized local random fields induced by Tb doping maximize the local converse piezoelectric response.

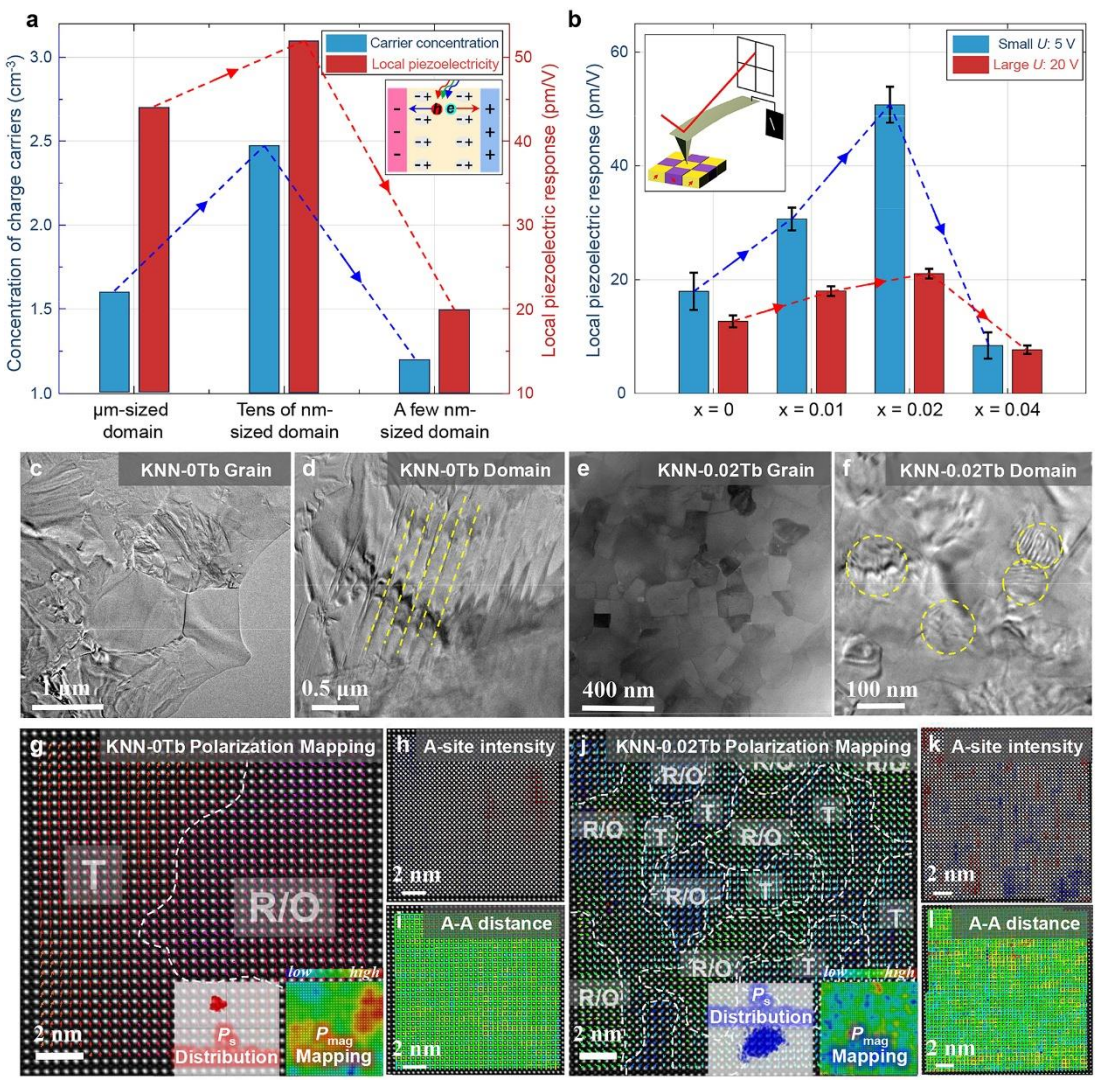

Fig. 3 | Enhanced optomechanical coupling in KNN-Tb ceramics. a, Relationship between ferroelectric domain sizes and the concentration of photocarriers on domain walls and the local piezoelectricity. The data were depicted as a function of domain size, derived from phase-field simulations on a photocarrier drift model within local ferroelectric domains. **b**, Local piezoelectric responses of KNN-*x*Tb ceramics under

large (20 V) and small (5 V) driving voltage conditions. Data were subtracted from the local switching spectroscopic PFM results. **c-f**, Grain and domain morphologies of KNN-0Tb and KNN-0.02Tb. **g-l**, Local polarization mapping and doping effect on A-site analysis on KNN-0Tb and KNN-0.02Tb samples.

To uncover the structural mechanisms underlying photostriction enhancement, we performed a multiscale microstructural analysis of KNN-Tb ceramics. With the increasing Tb concentration, grain sizes were reduced to tens-to-hundreds of nanometers range (Fig. S13), smaller than the incident modulated light wavelength (400 nm). Within these sub-nano-sized grains, domain sizes ranged from a few to tens of nanometers (Fig. S10), more than one order of magnitude below the visible light wavelength. Consistent with our design strategy, the tailored small grain and domain architecture effectively suppress light scattering and enhance optical transmission, facilitating more light-lattice interactions and ultimately yielding greater collective photostriction. To further investigate the local structural effects of Tb doping, we employed (S)TEM to characterize KNN-0Tb and KNN-0.02Tb. In agreement with SEM and PFM results, TEM images (Figs. 3c-3f) reveal a substantial reduction in both grain and domain sizes upon Tb incorporation. While rare-earth doping is a well-established strategy for tuning grain size and improving optical transparency in ferroelectric ceramics, its underlying mechanism for precisely and controllably modulating domain architecture remains unclear, posing a challenge for designing ferroelectrics with enhanced photostriction rate.

To gain deeper insight into domain evolution, we conducted local polarization mapping (Figs. 3g, 3j), analyzed the impact of Tb doping on A-site cations (Figs. 3h, 3i, 3k, 3l), and performed atomic-scale stress mapping (Fig. S14) on KNN-0Tb and KNN-0.02Tb. Compared to the well-aligned polarization vectors in KNN-0Tb, KNN-0.02Tb exhibits reduced polarization coherence, forming nanoscale domains (<10 nm) with small-angle domain walls. Consistent with phase-field simulations, smaller grains exhibit higher internal stress (Fig. S14), while increased Tb doping enhances local random fields (Fig. S15), leading to a domain size reduction from the micrometer to nanometer scale, with an intermediate domain size that can maximize the photo-induced strain (Figs. S16 and S17).

To further uncover effective strategies for controlling local photostriction in bulk ferroelectrics, we explored the underlying structural driving forces for regulating ferroelectric domains.

The composition-driven evolution of ferroelectric domains originates from changes in local spontaneous polarization, specifically, *DP* and P_{mag} (Fig. 4a). To uncover the atomic-scale driving forces for *DP* and P_{mag}, we conducted a statistical correlation analysis linking these polarization parameters to key microstructural factors, including A-site cation variations (reflected by A-site cation intensity variations),

oxygen octahedral tilt (*OT*), and oxygen octahedral distortion (*OD*). This analysis was based on atomic-scale mapping of these microstructural features, as provided in Figs. 4b and 4c (details can be seen in Supplementary Methods 1.3 and Figs. S18 and S19). Our analysis reveals a pronounced negative correlation between *DP* and P_{mag} (Fig. 4d), indicating that larger *DP* correspond to lower P_{mag}. This interdependence suggests a mutually competitive relationship between *DP* and P_{mag}. As provided in Figs. 4e and 4f, *OT* is correlated with *DP*, whereas *OD* is correlated with P_{mag}. Given that large *OD* characterizes domain walls, increasing *OT* thus serves as the primary driving force for reducing domain size. In contrast, increasing *OD* acts as the main driving force in enhancing P_{mag}.

To further elucidate the driving forces of evolving *OT* and *OD*, we statistically analyzed variations in the relative lengths of A–O and B–O bonds and correlated them with *OT* and *OD* (Figs. 4g and 4h). Fluctuation in B–O bond lengths positively correlates with *OD*, whereas variation in A–O bond lengths correlates positively with *OT*. These insights suggest that compositional adjustments targeting A–O and B–O bonds modifications could effectively tune *OD* and *OT*, thus balancing the competition between *DP* and P_{mag}. Under near-critical conditions, this strategy can achieve large *DP* while preserving relatively high P_{mag}. In size-reduced domains, each domain retains a high P_{mag}, promoting efficient drift of photocarrier toward domain walls. These charge carriers shield bound charges at domain walls, reduce depolarization fields, and thus facilitate rapid and enhanced local photostriction. Correlation coefficients among these local structural factors were provided in Fig. 4i, demonstrating the statistical reliability of our identified structural driving forces for modulating the domains.

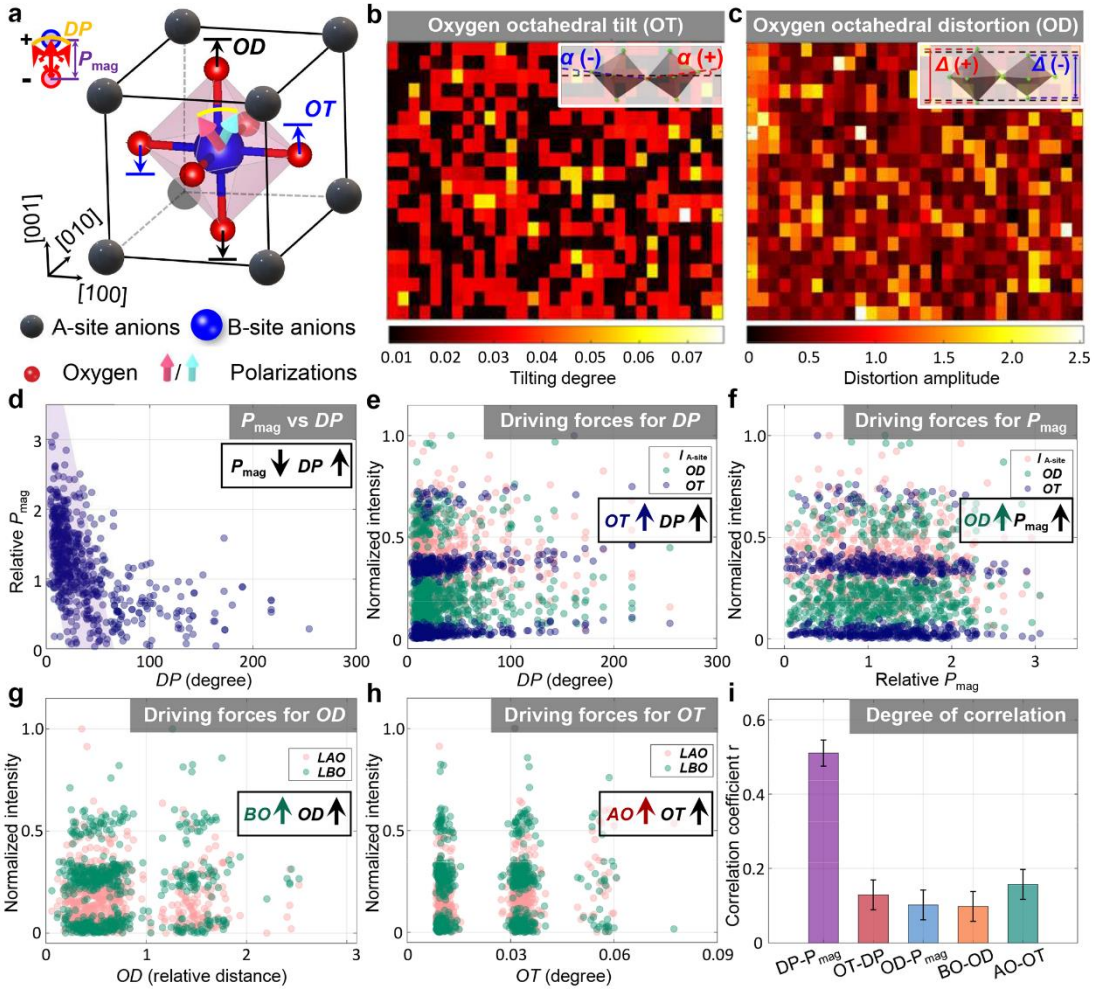

Fig. 4 | Structural driving force analysis for uncovering effective strategies to control photostriction in KNN-Tb. a, Grain and domain morphologies of KNN-*x*Tb. **b**, **c,** Key structural features and dominant driving forces governing domain evolution in perovskite materials. **d**, Correlation between polarization magnitude (P_{mag}) and polarization angle deviation (*DP*). **e**, Correlation among A-site cation intensity ($I_{A\text{-}site}$), oxygen octahedral tilt (*OT*), distortion (*OD*) and *DP*. **f**, Correlation among $I_{A\text{-}site}$, *OT*, *OD* and P_{mag}. **g**, Correlation between relative A-O (*LAO*) and B-O (*LBO*) bond lengths and *OD*. **h**, Correlation between *LAO* and *LBO* and *OT*. **i**, Degree of interdependence among local driving forces.

Opto-ultrasound Generation and Remote SHM via Photostriction

We designed a remote ultrasonic SHM system enabled by the photostricton in KNN-0.02Tb, to monitor the damage status of engineering structures[42]. The system employs a KNN-0.02Tb optomechanical cantilever transducer with the size of 0.25 mm × 0.50 mm × 3.00 mm (width × height × length), bonded to a 1.6 mm-thick aluminum plate (selection details in Supplementary Note 7). When illuminated by continuous light

modulated at 50.3 kHz corresponding to the resonance frequency of the coupled cantilever structure, the cantilever generates mechanical vibration due to photostriction in KNN-0.02Tb, exciting an ultrasonic wave propagating through the aluminum substrate. A laser scanning vibrometer captures the vibrational profiles, enabling real-time monitoring of defects, by analyzing amplitude and phase changes in the ultrasonic waves interacted with structural defects (Fig. 5a).

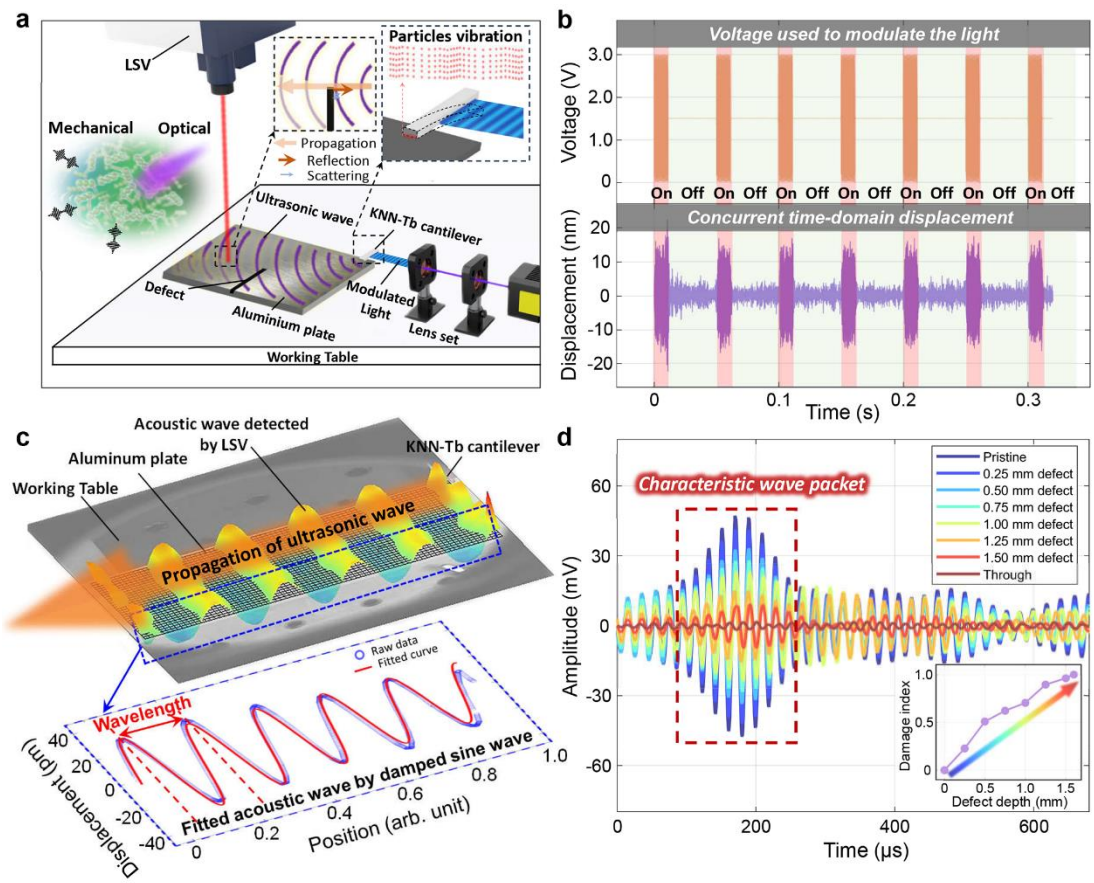

Fig. 5 | Opto-ultrasound generation and remote SHM by photostriction in non-poled KNN-Tb ceramics. a, Schematic of the remote ultrasonic SHM enabled by photostriction. Modulated light in continuous mode excites the KNN-*x*Tb cantilever that acts as an opto-ultrasonic transmitter, generating vibrations for exciting the ultrasound in the aluminum plate. The laser scanning vibrometer detects ultrasonic waves, with amplitude and phase of which indicating the location and size of structural defects in the aluminum plate. **b,** Reproducibility of the vibrations in the KNN-xTb cantilever, confirming its reliability as an ultrasonic transmitter. **c,** Ultrasonic wave propagation in the aluminum plate, excited by the cantilever's vibrations. The wave profile follows a damped sine function. **d,** Detection of defects with varying depths, demonstrating remote opto-ultrasonic SHM function. The received ultrasonic wave packet reveals signal reduction, quantified by the signal drop that increases with defect depth.

To assess reproducibility of this KNN-0.02Tb optomechanical transducer, cyclic on-off illumination tests were performed on it, with each "on" state inducing 500 electrical oscillations, repeated over seven on-off cycles (Fig. 5b). The results confirm the cantilever's reliability as an opto-mechanical transmitter. The system exhibited efficient wave coupling, producing ultrasonic signals with consistent periodicity (18.1 mm wavelength) and minimal attenuation across the pristine aluminum plate (Fig. 5c). Damped sine wave fitting ($R^2 > 0.95$) validated stable signal propagation, while spectral analysis confirmed frequency fidelity between the input modulation signals (50.3 kHz) and detected waveformsThe defect detection capability was evaluated using 4 mm × 22 mm strip defects of varying depths (0–1.6 mm), positioned 45 mm from the transmitter (Fig. S20). A 5-cycle, 3-V_{pp}, 50.3 kHz sine wave was applied to modulate the illumination on the KNN-0.02Tb transmitter, generating an A0 Lamb ultrasonic wave[43] detected by the laser scanning vibrometer (see determination in Fig. S21). The detected signal showed a clear reduction with increasing defect depth. To quantify this relation, we introduced a normalized damage index (DI)—based on residual signal energy method[44,45]—calculated from the amplitude difference of the characteristic wave packet between pristine and defected states (see Supplementary Note 8). The DI values show a consistent increase with defect depth until approaching the full plate thickness (inset of Fig. 5d). These results demonstrate the potential of non-poled KNN-Tb ceramics for remote opto-ultrasonic SHM applications.

Unlike conventional laser ultrasonics[46,47] or photoacoustic transducers[48-50] for SHM, which rely on optothermal expansion or plasma ablation under high peak-power pulsed illumination, our KNN–Tb cantilever leverages the ferroelectric photostrictive mechanism, where light drives strain via bulk photovoltaic effect and converse piezoelectricity. This non-thermal and cost-effective solid-state coupling enables reversible, safe, low-power opto-mechanical actuation, and excellent frequency control, attractive for many remote ultrasonic NDT and SHM systems, albeit with currently limited displacement amplitude compared to high-energy photoacoustic sources. By eliminating the complexity of the poling process and depoling issue during long-term monitoring operation, using the non-poled KNN-Tb offers a cost-effective approach with improved robustness in manufacturing the next-generation optomechanical devices.

In summary, we achieved an outstanding bulk photostriction rate of 6.41×10^{-1} s^{-1} in non-poled terbium-doped (K,Na)NbO_3 (KNN-Tb) ceramics, two orders of magnitude higher than typical bulk ferroelectrics. This exceptional performance results from the synergistic coupling between nanoscale bulk photovoltaic and converse piezoelectric effects, amplified by optimized optical penetration that promotes constructive accumulation of local photostriction. Atomic-resolution analyses reveal that A-site heavy hetero-ions

substitution modulates metal-oxygen bond lengths, tuning oxygen octahedral tilt (*OT*) and distortion (*OD*) level, and balancing polarization angle deviation (*DP*) and magnitude (P_{mag}). The competitive interplay between *DP* and P_{mag} fosters optimal ferroelectric domain configurations that facilitate efficient photocarrier drift to domain walls, enabling rapid and large local photostriction. Optimized optical penetration facilitates more grain participation in light–lattice interactions, promoting greater accumulation of local photostriction and enhancing the collective photostriction. The effective ultrasound generation and reliable remote SHM function are demonstrated, using an opto-ultrasonic cantilever transducer made from the KNN-Tb ceramics. Our research outcome here establishes a versatile strategy for engineering multiscale structures in bulk ferroelectrics, paving the way for cost-effective, high-performance opto-acoustic devices and providing a unique technical solution for remote opto-ultrasound applications.

Methods

See details of methods part in supplementary information files.

Data availability

The data generated in this study are provided in the Supplementary Information.

Code availability

MATLAB scripts are available from the first author and corresponding authors upon request.

Acknowledgements

The authors acknowledge the research grant supported by National Key R&D Program of China (2021YFB3201100), A*STAR-RIE2020 AME Industry Alignment Fund–Pre-positioning Programme (IAF-PP) (grant no. A20F5a0043), AME Programmatic Fund (Grant No. A20G9b0135), and IAF311014R, and by the National Natural Science Foundation of China (U23A20567, 2172128, 52172128 and 52472250). The authors acknowledge the technical support and discussions from TaiHang Laboratory and Zhejiang Shunhui Optical Technology Co., Ltd.

Author Contributions

J. Y. and K.Y. conceived the main idea. J. Y., H. W., J. W. and K. Y. designed and guided the experiments. Material selection, material fabrication by J. Y., H. T., C. Z. and C. L. Device design, improvement and testing by J. Y. The ultrasonic data processing and analysis were done by J. Y. X. S. conducted phase-field simulations. H. T. and J. Y. conducted the PFM characterization and analysis. H. W., Y. Y. and Y. Z. conducted the (S)TEM characterization and analysis, and J. Y. provided the correlation analysis script. D. B. K. L. and C. J. provided technical support for device fabrication and optimization. L. L., Y. S., X. D. and

J. S. provided technical support and discussions on the acoustic wave characterization by using the laser scanning vibrometer. J. Y., H. W., F. L., J. W. and K.Y. summarized and analyzed the data, and discussed the results. All authors contributed to discussing and writing the manuscript.

Competing interests

The authors declare no conflict of interest.

References

1. Chaikin, P. M.; Lubensky, T. C.; Witten, T. A., *Principles of condensed matter physics*. Cambridge university press Cambridge: 1995; Vol. 10.
2. Tang, S.-J.; Zhang, M.; Sun, J.; Meng, J.-W.; Xiong, X.; Gong, Q.; Jin, D.; Yang, Q.-F.; Xiao, Y.-F., Single-particle photoacoustic vibrational spectroscopy using optical microresonators. *Nature Photonics* **2023,** *17* (11), 951-956.
3. Vaia, R., Remote-controlled actuators. *Nature Materials* **2005,** *4* (6), 429-430.
4. Chen, X.; Kislyakov, I. M.; Wang, T.; Xie, Y.; Wang, Y.; Zhang, L.; Wang, J., Photoacoustic 2D actuator via femtosecond pulsed laser action on van der Waals interfaces. *Nature Communications* **2023,** *14* (1), 2135.
5. Gao, X.; Chen, X.; Hu, H.; Wang, X.; Yue, W.; Mu, J.; Lou, Z.; Zhang, R.; Shi, K.; Chen, X.; Lin, M.; Qi, B.; Zhou, S.; Lu, C.; Gu, Y.; Yang, X.; Ding, H.; Zhu, Y.; Huang, H.; Ma, Y.; Li, M.; Mishra, A.; Wang, J.; Xu, S., A photoacoustic patch for three-dimensional imaging of hemoglobin and core temperature. *Nature Communications* **2022,** *13* (1), 7757.
6. Kasatkina, L. A.; Ma, C.; Matlashov, M. E.; Vu, T.; Li, M.; Kaberniuk, A. A.; Yao, J.; Verkhusha, V. V., Optogenetic manipulation and photoacoustic imaging using a near-infrared transgenic mouse model. *Nature communications* **2022,** *13* (1), 2813.
7. Liang, Y.; Sun, H.; Cheng, L.; Jin, L.; Guan, B.-O., High spatiotemporal resolution optoacoustic sensing with photothermally induced acoustic vibrations in optical fibres. *Nature Communications* **2021,** *12* (1), 4139.
8. Pan, J.; Li, Q.; Feng, Y.; Zhong, R.; Fu, Z.; Yang, S.; Sun, W.; Zhang, B.; Sui, Q.; Chen, J.; Shen, Y.; Li, Z., Parallel interrogation of the chalcogenide-based micro-ring sensor array for photoacoustic tomography. *Nature Communications* **2023,** *14* (1), 3250.
9. Forsch, M.; Stockill, R.; Wallucks, A.; Marinković, I.; Gärtner, C.; Norte, R. A.; van Otten, F.; Fiore, A.; Srinivasan, K.; Gröblacher, S., Microwave-to-optics conversion using a mechanical oscillator in its quantum ground state. *Nature Physics* **2020,** *16* (1), 69-74.
10. Chen, Y.-S.; Zhao, Y.; Yoon, S. J.; Gambhir, S. S.; Emelianov, S., Miniature gold nanorods for photoacoustic molecular imaging in the second near-infrared optical window. *Nature Nanotechnology* **2019,** *14* (5), 465-472.
11. Vogele, A.; Sonner, M. M.; Mayer, B.; Yuan, X.; Weiß, M.; Nysten, E. D.; Covre da Silva, S. F.; Rastelli, A.; Krenner, H. J., Quantum dot optomechanics in suspended nanophononic strings. *Advanced Quantum Technologies* **2020,** *3* (2), 1900102.
12. Li, B. B.; Brawley, G.; Greenall, H.; Forstner, S.; Sheridan, E.; Rubinsztein-Dunlop, H.; Bowen, W. P., Ultrabroadband and sensitive cavity optomechanical magnetometry. *Photonics Research* **2020,** *8* (7), 1064–1071.
13. Qian, H.; Fan, Z.-Y.; Li, J., Entangling mechanical vibrations of two massive ferrimagnets by fully exploiting the nonlinearity of magnetostriction. *Quantum Science and Technology* **2022,** *8* (1), 015022.
14. Kobyakov, A.; Sauer, M.; Chowdhury, D., Stimulated Brillouin scattering in optical fibers. *Advances in*

optics and photonics **2009,** *2* (1), 1–59.
15. Liu, Q.; Li, H.; Li, M., Electromechanical Brillouin scattering in integrated optomechanical waveguides. *Optica* **2019,** *6* (6), 778–785.
16. Ma, Y.; Liang, T.; Qiao, S.; Liu, X.; Lang, Z., Highly sensitive and fast hydrogen detection based on light-induced thermoelastic spectroscopy. *Ultrafast Science* **2023,** *3*, 0024.
17. Rosencwaig, A.; Gersho, A., Theory of the photoacoustic effect with solids. *Journal of Applied Physics* **1976,** *47* (1), 64-69.
18. Mogunov, I. A.; Lysenko, S.; Fedianin, A. E.; Fernández, F. E.; Rúa, A.; Kent, A. J.; Akimov, A. V.; Kalashnikova, A. M., Large non-thermal contribution to picosecond strain pulse generation using the photo-induced phase transition in VO_2. *Nature Communications* **2020,** *11* (1), 1690.
19. Yu, Y.; Nakano, M.; Ikeda, T., Directed bending of a polymer film by light. *Nature* **2003,** *425* (6954), 145-145.
20. Lejman, M.; Vaudel, G.; Infante, I. C.; Gemeiner, P.; Gusev, V. E.; Dkhil, B.; Ruello, P., Giant ultrafast photo-induced shear strain in ferroelectric $BiFeO_3$. *Nature Communications* **2014,** *5* (1), 4301.
21. Kundys, B.; Viret, M.; Colson, D.; Kundys, D. O., Light-induced size changes in $BiFeO_3$ crystals. *Nature Materials* **2010,** *9* (10), 803-805.
22. Liew, W. H.; Chen, Y.; Alexe, M.; Yao, K., Fast photostriction in ferroelectrics. *Small* **2022,** *18* (7), 2106275.
23. Tian, H.; Ren, T.-L.; Xie, D.; Wang, Y.-F.; Zhou, C.-J.; Feng, T.-T.; Fu, D.; Yang, Y.; Peng, P.-G.; Wang, L.-G., Graphene-on-paper sound source devices. *ACS Nano* **2011,** *5* (6), 4878-4885.
24. Cheng, F.; Zhang, Y.; Yin, R.; Yu, Y., Visible light induced bending and unbending behavior of crosslinked liquid-crystalline polymer films containing azotolane moieties. *Journal of Materials Chemistry* **2010,** *20* (23), 4888-4896.
25. Yue, Y.; Norikane, Y.; Azumi, R.; Koyama, E., Light-induced mechanical response in crosslinked liquid-crystalline polymers with photoswitchable glass transition temperatures. *Nature Communications* **2018,** *9* (1), 3234.
26. Ji, S.; Fan, F.; Sun, C.; Yu, Y.; Xu, H., Visible light-induced plasticity of shape memory polymers. *ACS Applied Materials Interfaces* **2017,** *9* (38), 33169-33175.
27. Lendlein, A.; Jiang, H.; Jünger, O.; Langer, R., Light-induced shape-memory polymers. *Nature* **2005,** *434* (7035), 879-882.
28. Wang, S.; Urban, M. W., Self-healing polymers. *Nature Reviews Materials* **2020,** *5* (8), 562-583.
29. Xia, Y.; He, Y.; Zhang, F.; Liu, Y.; Leng, J., A review of shape memory polymers and composites: mechanisms, materials, and applications. *Advanced Materials* **2021,** *33* (6), 2000713.
30. Wissmeyer, G.; Pleitez, M. A.; Rosenthal, A.; Ntziachristos, V., Looking at sound: optoacoustics with all-optical ultrasound detection. *Light: Science Applications* **2018,** *7* (1), 53.
31. Dubois, M.; Drake Jr, T. E., Evaluation, Evolution of industrial laser-ultrasonic systems for the inspection of composites. *Nondestructive Testing Evaluation* **2011,** *26* (3-4), 213-228.
32. Lv, G.; Guo, S.; Chen, D.; Feng, H.; Zhang, K.; Liu, Y.; Feng, W., Laser ultrasonics and machine learning for automatic defect detection in metallic components. *NDT E International* **2023,** *133*, 102752.
33. Ren, D.; Li, C.; Shi, J.; Chen, R., A review of high-frequency ultrasonic transducers for photoacoustic imaging applications. *IEEE Transactions on Ultrasonics, Ferroelectrics, and Frequency Control* **2021,** *69* (6), 1848-1858.
34. Lin, L.; Wang, L. V., The emerging role of photoacoustic imaging in clinical oncology. *Nature Reviews Clinical Oncology* **2022,** *19* (6), 365-384.
35. Chen, X.; Zhao, Y.; Ahmad, N.; Zhao, J.; Zheng, Z.; Su, Z.; Peng, X.; Li, X.; Zhang, X.; Fan, P., Achieving high open-circuit voltage in efficient kesterite solar cells via lanthanide europium ion induced carrier lifetime enhancement. *Nano Energy* **2024,** *124*, 109448.
36. Yin, J.; Shi, X.; Tao, H.; Tan, Z.; Lv, X.; Ding, X.; Sun, J.; Zhang, Y.; Zhang, X.; Yao, K.; Zhu, J.; Huang, H.; Wu, H.; Zhang, S.; Wu, J., Deciphering the atomic-scale structural origin for large dynamic electromechanical response in lead-free $Bi_{0.5}Na_{0.5}TiO_3$-based relaxor ferroelectrics. *Nature*

Communications **2022,** *13* (1), 6333.
37. Carrera, E.; Giunta, G.; Petrolo, M., *Beam structures: classical and advanced theories*. John Wiley & Sons, 2011.
38. Coble, R.; Kingery, W., Effect of porosity on physical properties of sintered alumina. *Journal of the American Ceramic Society* **1956,** 39(11), 377–385.
39. Paillard, C.; Xu, B.; Dkhil, B.; Geneste, G.; Bellaiche, L. J. P. r. l., Photostriction in ferroelectrics from density functional theory. *Physical Review Letters* **2016,** *116* (24), 247401.
40. Kumar, A.; Baker, J. N.; Bowes, P. C.; Cabral, M. J.; Zhang, S.; Dickey, E. C.; Irving, D. L.; LeBeau, J. M., Atomic-resolution electron microscopy of nanoscale local structure in lead-based relaxor ferroelectrics. *Nature materials* **2021,** *20* (1), 62-67.
41. Yin, J.; Zong, H.; Tao, H.; Tao, X.; Wu, H.; Zhang, Y.; Zhao, L.-D.; Ding, X.; Sun, J.; Zhu, J.; Wu, J.; Pennycook, S. J., Nanoscale bubble domains with polar topologies in bulk ferroelectrics. *Nature Communications* **2021,** *12* (1), 1-8.
42. Yin, J.; Wong, V. K.; Xu, Q.; Subhodayam, P. T. C.; Yousry, Y. M.; Shashidhara, A.; Zhou, J.; Luo, P.; Lim, P. C.; Wei, F.; Lim, D. B. K.; Sun, C.; Yao, K., Conformable shear mode transducers from lead-free piezoelectric ceramic coatings: an innovative ultrasonic solution for submerged structural health monitoring. *Advanced Functional Materials* **2024,** *34* (32), 2401544.
43. Shen, Z.; Chen, S.; Zhang, L.; Yao, K.; Tan, C. Y., Direct-write piezoelectric ultrasonic transducers for non-destructive testing of metal plates. *IEEE Sensors Journal* **2017,** *17* (11), 3354-3361.
44. Yousry, Y. M.; Wong, V. K.; Ji, R.; Chen, Y.; Chen, S.; Zhang, X.; David, B. K. L.; Yao, K., Shear mode ultrasonic transducers from flexible piezoelectric PLLA fibers for structural health monitoring. *Advanced Functional Materials* **2023,** *33* (15), 2213582.
45. Su, Z.; Ye, L., *Identification of damage using lamb waves: from fundamentals to applications*. Vol. 48 (Springer Science & Business Media, 2009).
46. Xie, L.; Lian, Y.; Du, F.; Wang, Y.; Lu, Z., Optical methods of laser ultrasonic testing technology in the industrial and engineering applications: A review. *Optics & Laser Technology* **2024,** *176*, 110876.
47. Quintero, R.; Simonetti, F.; Howard, P.; Friedl, J.; Sellinger, A., Noncontact laser ultrasonic inspection of ceramic matrix composites (CMCs). *NDT & E International* **2017,** *88*, 8-16.
48. Chen, S. L.; Tian, C., Recent developments in photoacoustic imaging and sensing for nondestructive testing and evaluation. *Visual Computing for Industry, Biomedicine, and Art* **2021,** *4*(1), 6.
49. Glorieux, C., Perspective on non-invasive and non-destructive photoacoustic and photothermal applications. *Journal of Applied Physics* **2022,** *131*(17), 170903.
50. Wang, S.; Echeverry, J.; Trevisi, L.; Prather, K.; Xiang, L.; Liu, Y., Ultrahigh resolution pulsed laser-induced photoacoustic detection of multi-scale damage in CFRP composites. *Applied Sciences* **2020,** *10*(6), 2106.

Editor's summary:

Hierarchical nanostructures in ferroelectric ceramics greatly enhance light-driven strain, yielding a photostriction rate two orders higher than conventional bulk materials and enabling remote ultrasonic sensing for structural health monitoring.

Peer review information: *Nature Communications* thanks Lars Hoff, Pascal Ruello and the other anonymous reviewer(s) for their contribution to the peer review of this work. A peer review file is available.